A GPS water vapor tomography method based on a genetic algorithm

Fei Yang[1,2,3,4], Jiming Guo[1,3,4*], Junbo Shi[1,3*], Xiaoling Meng[2], Yinzhi Zhao[1], Lv Zhou[5] and Di Zhang[1]

[1]School of Geodesy and Geomatics, Wuhan University, Wuhan 430079, China;

[2]Nottingham Geospatial Institute, University of Nottingham, Nottingham NG7 2TU, United Kingdom

[3]Key Laboratory of Precise Engineering and Industry Surveying of National Administration of Surveying, Mapping and Geoinformation, Wuhan University, Wuhan 430079, China;

[4]Research Center for High Accuracy Location Awareness, Wuhan University, China ;

[5]Guilin University of Technology, Guilin 541004, China.

Correspondence to: Jiming Guo and Junbo Shi (jmguo@sgg.whu.edu.cn; jbshi@sgg.whu.edu.cn.)

Abstract. Water vapor is an important substituent of atmosphere, but its spatial and temporal distribution is difficult to detect. Global Positioning System (GPS) water vapor tomography, which can sense three-dimensional water vapor distribution, has been developed as a research area in the field of GPS meteorology. In this paper, a new water vapor tomography method based on a genetic algorithm (GA) is proposed to overcome the ill-conditioned problem. The proposed approach does not need to perform matrix inversion, and it does not rely on excessive constraints, a priori information and external data. Experiments in Hong Kong under rainy and rainless conditions using this approach show that a serious ill-conditioned problem in the tomographic matrix by grayscale and condition numbers. Numerical results show that the average root mean square error (RMS) and mean absolute error (MAE) for internal and external accuracy are 1.52/0.94 mm and 10.07/8.44 mm, respectively, with the GAMIT-estimated slant water vapor (SWV) as a reference. Comparative results of water vapor density (WVD) derived from radiosonde data reveal that the tomographic results based on GA with a total RMS/MAE of 1.43/1.19 mm are in good agreement with that of radiosonde measurements. In comparison to the traditional Least squares method, the GA can achieve a reliable tomographic result with high accuracy without the restrictions mentioned-above. Furthermore, the tomographic results in a rainless scenario are better than those of a rainy scenario, and the reasons are discussed in detail in this paper.

1 Introduction

Water vapor is a major component of the atmosphere and its distribution and dynamics are the main driving force of weather and climate change. A good understanding of water vapor is crucially important for meteorological applications and research such as severe weather forecasting and warnings (Liu et al., 2005). Nevertheless, the variation of water vapor is affected by many factors including, temperature, topography and seasons with characteristics of changing fast with time and heavily in vertical and horizontal directions, which makes it difficult to monitor with high temporal and spatial resolutions (Rocken et al., 1993).

Thanks to the development of GPS station networks providing atmospheric information under all weather conditions, GPS is considered as a powerful technique to retrieve water vapor. Since Bevis et al. (1992) first envisioned the potential of tomography applying in GPS meteorology, water vapor tomography has become a promising method to improve the restitution of the spatio-temporal variations of this parameter (Braun et al., 1999; Nilsson et al., 2004; Song et al., 2006; Perler et al., 2011; Rohm, 2012; Dong and Jin, 2018).

In GPS water vapor tomography, the research area should be covered by ground GPS receivers and discretized into a number of cubic closed voxels by latitude, longitude and altitude, each of which has a fixed amount of water vapor at a particular time (Guo et al., 2016). The observations are GPS-derived slant water vapor, the precipitable water in the direction of the signal ray-path, which travels through the troposphere from its top (Zhao and Yao, 2017). After obtaining the precise measurement of the signal ray distance in each voxel by raytracing its path from receiver to satellite, we can achieve the basic equation for water vapor tomography, which can be expressed in linear form (Flores et al., 2000; Yang et al., 2018):

$$SWV^q = \sum_{i=1}^{n} d_i^q \cdot x_i, \tag{1}$$

where the superscript q is the satellite signal index, SWV^q denotes the qth slant water vapor achieved by GPS tropospheric estimation, n is the total number of tomographic voxels discretized. d_i^q denotes the distance of qth signal ray inside voxel i which can be obtained by the satellite and station coordinates, and x_i is the water vapor density of voxel i. Using all suitable SWV observations, we can form the tomographic observation equation:

$$y_{m \times 1} = A_{m \times n} \cdot x_{n \times 1}, \tag{2}$$

where y is a column vector of SWV, m is the total number of SWV measurements in tomography, A denotes the intercept matrix containing the distance of the signal ray in each of the voxels, n is the number of voxels in the study area, and x denotes the vector of the unknown water vapor density.

Since a GPS signal ray can only pass through a small part of the voxels in the study area, the elements of matrix A are likely to be equal to zero, making it a large sparse matrix. In addition, the effective signal rays will concentrate around the zenith due to the unfavourable geometry of the GPS stations and the special structures of the satellites. These all make Eq. (2) ill-conditioned, and it is difficult to obtain the unknowns by performing the inversion of Eq. (2), in the form of $x = A^{-1} \cdot y$.

To circumvent the ill-conditioned problem, many methods are explored in the literature. Flores et al. (2000) added constraints on the vertical and horizontal variability of tomography with additional top constraints to the model. Most constraints are based on experiences and difficult to match to the actual water vapor distribution, resulting in the deviation of tomographic results. Moreover, singular value decomposition (SVD) is required to perform matrix inversion. Bender et al. (2011) utilized an iterative algorithm called algebraic reconstruction technique (ART) to solve the observation equation. Several reconstruction algorithms of the ART family were also implemented, e.g. the multiplicative algebraic reconstruction

techniques (MART) and the simultaneous iterations reconstruction technique (SIRT) (Stolle et al., 2006; Liu et al., 2010). The ART techniques are iterative algorithms that proceed observation by observation. Only two vectors y, x and a data structure containing the slant subpaths in each voxel are required to solve the observation equations. The algorithms consist of two loops. The inner loop processes SWV by SWV and applies an adequate correction to each voxel. SWVs that execute the next iteration start in the outer loop (Bender et al., 2011). Perform the matrix inversion I not necessary, thus avoiding the ill-conditioned problem. However, only the results of the voxels that travelled through via signal rays are updated, and the tomographic results heavily depend on the exact initial field, the data quality and relaxation parameter (Wang et al., 2014). Nilsson and Gradinarsky (2004) adapted a Kalman filter approach to estimate tomographic results without adding constraints and performing inversion. This approach assumes that the water vapor density in each voxel meets the Gauss-Markov random walk pattern for a certain period of time, and establishes the corresponding state equation of Kalman Filter. The used observation vector is based on the mathematical model to perform the optimal estimation of the state vector, which is a process of continuous prediction and correction. In this method, initializing the filter with an informed estimation of the water vapor field and providing the initial covariance of state equation are based on external data. Other approaches that enrich the information of the observation equation were exploited in recent years, including the Constellation Observing System for Meteorology, Ionosphere, and Climate (COSMIC) occultation data by Xia et al. (2013), Interferometric Synthetic Aperture Radar (InSAR) by Benevides et al. (2015), water vapor radiometer (WVR) and numerical weather prediction by Chen and Liu (2016).

In the above-mentioned tomographic methods, excessive constraints with the matrix inversion, an exact priori information or external data are commonly used to overcome the ill-conditioned problem. The mandatory usage of excessive constraints in tomographic experiments with poor voxel structure will induce limitations, while reliance on an exact priori information will make the tomographic solutions too similar to the priori data and decrease the role of the tomography technique. External data cannot be used in all tomographic experiments. Therefore, this paper proposes a new tomography method based on a genetic algorithm (Section 2). The tomography experiments and results of the analysis are presented in Section 3. Section 4 summarizes the conclusions.

2 Methodology

2.1 Troposphere estimation

In water vapor tomography, the observation is slant water vapor which can be converted from slant wet delay (SWD) by the following formula (Adavi and Mashhadi, 2015):

$$SWV = \Pi \times SWD = \frac{10^6}{\rho_w \times \dfrac{R}{m_w}\left(\dfrac{k_3}{T_m} + k_2 - \dfrac{m_w}{m_d} \times k_1\right)} \times SWD, \tag{3}$$

where Π denotes conversion factor. $k_1 = 77.604 K \cdot hPa^{-1}$, $k_2 = 70.4 K \cdot hPa^{-1}$, $k_3 = 3.775 \times 10^5 K^2 \cdot hPa^{-1} \cdot \rho_w$ is the liquid water density (unit: g/m³), $R = 8314 Pa \cdot m^3 \cdot K^{-1} \cdot kmol^{-1}$ represents the universal gas constant, $m_w = 18.02 kg \cdot kmol^{-1}$ and $m_d = 28.96 kg \cdot kmol^{-1}$ indicate the molar mass of water and the dry atmosphere, respectively. T_m denotes the weighted mean temperature which is the ratio of two vertical integrals though the atmosphere (Davis et al., 1985). In practice, an empirical formula is used to achieve approximate T_m by surface temperature T_s in K ($T_m = 85.63 + 0.668 T_s$) (Liu et al., 2001; Astudillo et al., 2018). SWD can be obtained as follows (Zhang et al., 2017):

$$SWD = f(ele) \times ZWD + f(ele) \times \cot(ele) \times \left(G_{NS}^w \times \cos(azi) + G_{WE}^w \times \sin(azi)\right) + R, \qquad (4)$$

where ele and azi are the satellite elevation and azimuth, respectively. f denotes the wet mapping function, G_{NS}^w and G_{WE}^w refer to the wet delay gradient parameters in the north-south and east-west direction, respectively. R is the unmodelled atmospheric slant delay, which is included in the zero-differences residuals. ZWD represents zenith wet delay, which is the wet component of zenith total delay (ZTD) affected by water vapor along the satellite signal ray. It can be separated from ZTD by subtracting the zenith hydrostatic delay (ZHD). The ZTD is the primary parameter retrieve with GPS and spatially averaged parameter. If pressure measurements are available, the ZHD is calculated by the Saastamoinen model as follows (Saastamoinen, 1972):

$$ZHD = \frac{0.002277 \times P_s}{1 - 0.00266 \times \cos(2\varphi) - 0.00028 \times H}, \qquad (5)$$

where P_s refers to the surface pressure, φ and H represent the latitude and the geodetic height of the station, respectively.

2.2 Water vapor tomography based on Least squares method

After obtaining the observation equation (Eq. (2)), three types of constraints are usually added:

$$0 = H \cdot x, \qquad (6)$$

$$0 = V \cdot x, \qquad (7)$$

$$0 = T \cdot x \qquad (8)$$

Equations (6)-(8) are the vertical, horizontal and top constraints, respectively. The horizontal constraint equation assumes that the distribution of water vapor density is relatively stable in the horizontal direction within a small region. Thus, the water vapor density within a certain voxel can be represented by the weighted average of its neighbouring voxels in the same layers. The vertical constraint equation is a relationship established for the voxels between two adjacent layers based on the analysis of meteorological data for many years. The top constraint is obtained by setting the water vapor density of the top

boundary to a small constant. Based on the principle of Least square, the tomographic results can be achieved by the following formula:

$$x = \left(A^T A + H^T H + V^T V + T^T T \right)^{-1} \times \left(A^T y \right) \tag{9}$$

To obtain the inverse matrix in Eq. (9), the singular value decomposition is required. More details on this technique can be found in e.g. Flores et al. (2000).

2.3 Water vapor tomography based on the genetic algorithm

For water vapor tomography based on the genetic algorithm, the first procedure is to construct the tomographic equation. The idea of function optimization is then used to solve Eq. (2) (Guo and Hu, 2009; Olinsky et al., 2004), which is similar to the principle of Least squares $V^T PV = \min$ (Flores et al., 2000). Eq. (2) can be converted into the form as follows:

$$\min f(\mathrm{x}) = \left(y - Ax \right)^T P \left(y - Ax \right), x \in R+, \tag{10}$$

where the terms are the same as in Eq. (2). In this equation, the values of x that minimize function $f(x)$ are the result of tomography. To achieve the best values of x, the traditional method adopts a derivative method which needs matrix inversion in the follow-up. Genetic algorithm, which was first introduced by Holland (1992), provides an adaptive search method to achieve the tomographic results. It is designed to simulate the evolutionary processes in the nature, in which the principle of survival of the fittest is applied to produce better and better approximates to the function. Eq. (10) is regarded as the fitness function that is used to measure the performance of the searched values of x by computing the fitness value (Goldberg, 1989; Venkatesan et al., 2004). Through searching generation after generation, the water vapor result that best fits the function can be found. The specific steps of water vapor tomography based on genetic algorithm are as follows:

1) Construct the fitness function which is converted from the tomographic equation.
2) Generate some groups representing approximates of x (water vapor density) stochastically, which form the initial population.
3) Select groups from the last generation of the population as parents according to a lower to higher order of the groups of x corresponding to their fitness values.
4) Produce offspring groups from parents by crossover and mutation to make up a new set of approximated solution (new generation).
5) Compute the fitness values of the new generation, go back to step 3) and produce the next generation of the population.
6) The search terminates when a group of approximates meets the requirements of the fitness value. Generally, we set the stopping criteria for generation or calculation time.

The parameters of genetic algorithm are listed in Table 1 (Wang et al., 2010). Roulette is a function used for selection in step 3), referring to the concept of a roulette wheel in which the area of each segment is proportional to its expected value and

one of the sections is selected with a random number whose probability equals its area. For the crossover function, Intermediate in Table 1 is intended to create offspring groups by a random weighted average of the parents. The mutation process forces the individuals in the population to undergo small random changes that enable the genetic algorithm to search a wider space. Adaptive feasibility is chosen for the mutation function, which means that the adaptive direction is generated randomly with respect to the last successful or unsuccessful generation (Dwivedi and Dikshit, 2013). Based on these steps, the optimal solution of Eq. (10) is derived, that is, the value of x that gives $f(x)$ the minimum value, and also the value of water vapor density in the tomographic equations. To more clearly show the process of water vapor tomography based on genetic algorithm, the flowchart is shown in Fig.1.

Table 1. Parameters of the genetic algorithm

Parameter	Strategy
Population Size	200
Crossover Fraction	0.8
Reproduction of Elite Count	10
Selection Function	Roulette
Crossover Function	Intermediate
Mutation Function	Adaptive Feasibility
Generations of Stopping Criteria	100*Number of Variables
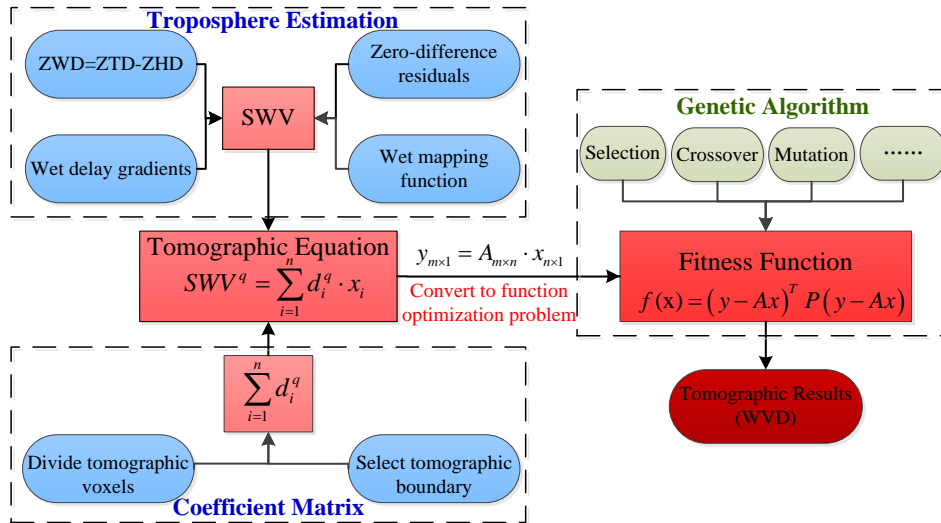
Fig.1 Flowchart of the water vapor tomography based on the genetic algorithm

3 Experiment and Analysis

3.1 Experiment Description
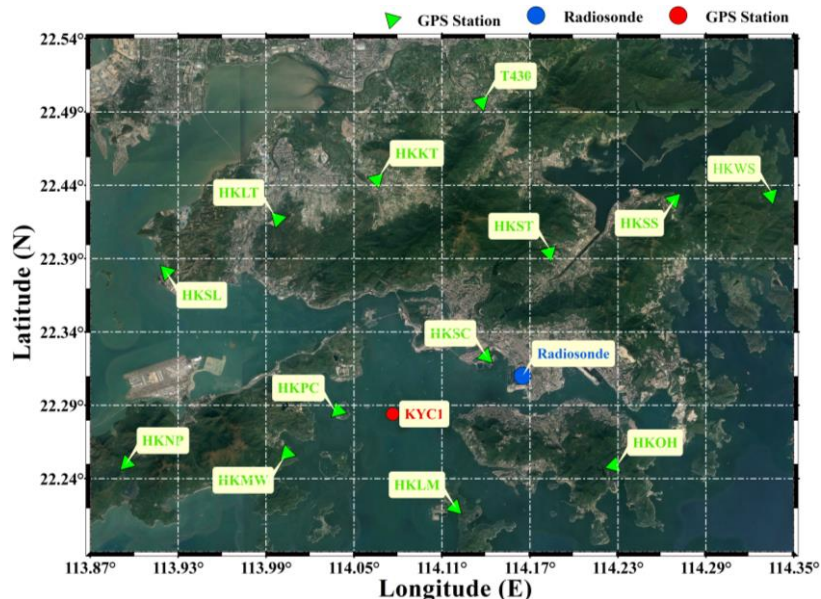
Fig. 2 Geographic distribution of GPS, radiosonde stations and the horizontal structure of the voxels used in water vapor tomography. Map data ©2018 Google.

In order to conduct the tomographic experiment based on genetic algorithm, Hong Kong was selected as the research region. The boundary and resolution in west-east and south–north direction were 113.87°-114.35°, 0.06° and 22.19°-22.54°, 0.05°, respectively. For the altitude direction, 0-8.0 km and 800 m were chosen. A total of $8 \times 7 \times 10$ voxels in the tomography grid was obtained. As shown in Figure 2, thirteen GPS stations of the Hong Kong Satellite Positioning Reference Station Network (green triangle) were selected in the tomography modelling to provide SWV measurements. Another GPS station (KYC1, red spot) and radiosonde station (45005, blue spot) were used to check the result of tomography. Each GPS station recorded temperature, pressure and relative humidity by an automatic meteorological device, by which the hydrostatic parts of the troposphere delay can be accurately achieved. All the stations are under 400 m and located in the first layer of the tomographic grids.

The GPS tropospheric parameters (zenith tropospheric delay and gradient parameters) were estimated by the GAMIT 10.61 software based on a double-differenced model. In order to reduce the strong correlation of tropospheric parameters caused by the short baseline between GPS receivers in the tomographic area, three International GNSS Service (IGS) stations (GJFS, LHAZ and SHAO) were incorporated into the solution model. In the processing, the sampling rate of observations was 30s, a cut-off elevation angle of 10° was selected, and the IGS precise ephemeris was adopted. The LC_AUTCLN and BASELINE modes were selected as the processing strategies, representing that the GPS observation was the ionosphere-free linear combination and the orbital parameters were fixed, respectively. The tropospheric parameters, including troposphere delay

gradients and ZTD at 4-h and 2-h intervals, are estimated and interpolated to 30s sampling rate in the GAMIT software. Note that the outputs of the GAMIT are double-differenced residuals and troposphere delay gradients. To obtain the R in Eq. (4), double-differenced residuals should be converted to zero-differences residuals and multipath effects should be considered by the method proposed by Alber et al. (2000). To achieve the wet delay gradients, Bar-Sever et al. (1998) considered the

5   average of troposphere gradients within 12 hours as the dry delay gradients and subtracted it from the troposphere delay gradients. Then all the necessary parameters are available for Eq. (4) to build SWD, and SWV was obtained by Eq. (3).

To verify the proposed method, two periods of GPS observation data, with a sampling rate of 30s, were used in the tomography experiment. One from 13 to 19 August, 2017 (DOY of 225 to 231, 2017), during which a spell of fine weather prevailed in Hong Kong with a ridge of high-pressure extending westwards from the Pacific to cover south-eastern China on

10 16-18 August. In this period of time, the daily rainfall is 0 mm. Moreover, the relative humidity and SWV produced in the selected stations on average are 75% and 79.1 mm, respectively. This period is defined as rainless days. Hence, fine weather occurs without any rainfall. In addition, the relative humidity and SWV are small. The other period is from 12 to 18 June, 2017 (DOY of 163 to 169, 2017), which covers the rainy days. During the selected rainy period, the weather of Hong Kong was first affected by the approach and the passage of a severe tropical storm, named Merbok, with more than 150 mm of

15 rainfall recorded on 13-14 June. Thereafter, from 15 and 16 June, the influence of an enhanced southwest monsoon and the development of a lingering through of low pressure made the weather remaining unstable and rainy till 21 June. In this period of time, the maximum daily rainfall is up to 203.7 mm, and the average daily rainfall is 66.8 mm. The average relative humidity and SWV produced in the selected stations are 89% and 112.9 mm, respectively. This period represents as rainy days, indicating that continuous rainfall occurs, and the relative humidity and SWV are high. The period covered is 0.5h for

20 each tomographic solution. The radiosonde data, collected twice daily at 00:00 and 12:00 UTC in these two periods, were treated as reference data.

According to the flowchart presented in Fig. 1, the above GPS observation data were processed to construct the tomographic equation and further convert it into the fitness function for the optimization algorithm. Population size is chosen based on the total number of unknown parameters (water vapor density). The value of 200 is the default option of the algorithm when the

25 number of unknows exceeds a certain amount. The reproduction of elite count is chosen to be 10 to specify the number of individuals that are guaranteed to survive to the next generation because it is based on population size (0.05 * population size). The crossover fraction is set to the default value of 0.8 to specify the fraction of the next generation that crossover produces. In this study, generation is chosen as the stopping criteria and 100*Number of Variables is the default. Other parameters, including roulette, intermediate and adaptive feasibility, are selected because they are the most commonly used

30 settings for genetic algorithms. Other selection functions as well as crossover and mutation functions can be adopted in the genetic algorithm. In addition, population size, crossover fraction, elite count and stopping criteria can also be set to other values which may slightly affect solution time and results. The specific impact can be explored in depth in future research.

3.2 Analysis of matrix ill-condition

In a tomographic solution, the structure of the coefficient matrix in the observation equation depends on which voxels are crossed by SWV and the number of signal rays penetrating each voxel. Fig. 3 illustrates this in the form of a grayscale graph for two different days: 13 August, 2017 at UTC 00:00, a rainless day (a), and 13 June, 2017 at UTC 12:00, a rainy day (b). In the upper panel of each graph, the deepening of the grayscale refers to an increase in the number of signal rays crossing through the voxel. The closer the layer to the ground, the more voxels are not crossed by any signal rays. Although there are few voxels with no signal rays passing through in the upper layers, many of the voxels have a lighter grayscale which means that the voxels are crossed by fewer signal rays.

Note that when the signal ray passes vertically through the tomographic region, the ray crossed a minimum number of voxels, that is, ten in the tomographic area. Therefore, the minimum probability that a voxel will be crossed by a ray is 1.79% (10/560, 560 is the total number of the voxels in this tomographic experiment). Thus 1.79% of the total SWV is taken as a criteria to further illustrate the structure of the coefficient matrix. If the number is greater than the threshold, the voxel is considered to be crossed by sufficient rays, otherwise the voxel is defined as an insufficient one. For the two examples shown, the number of total SWV and the criteria are 4930/4569 and 88/81, respectively. The lower panel of each graph displays the distribution of sufficient (black rectangle) and insufficient (white rectangle) ones. Obviously, many voxels are not crossed by enough satellite rays, both for the upper layers or the lower layers.
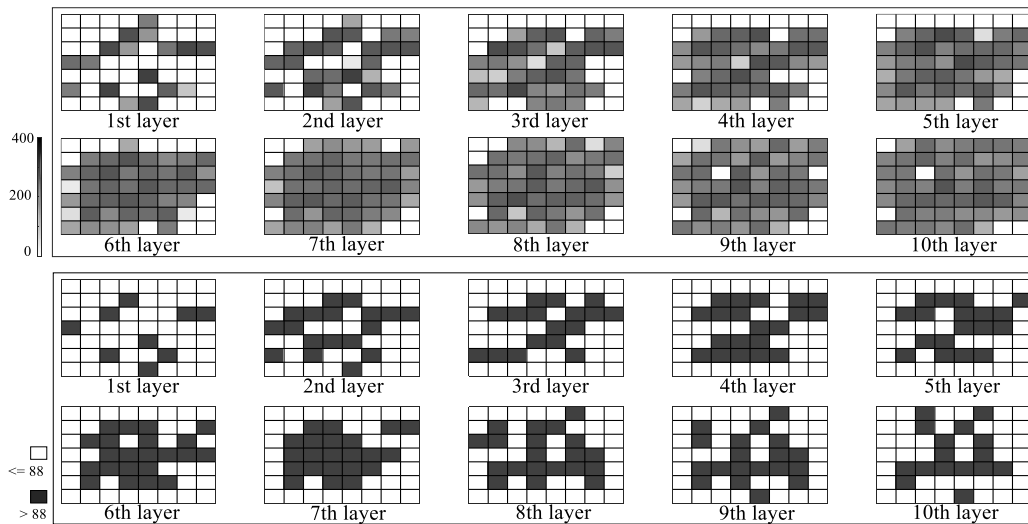
(a)
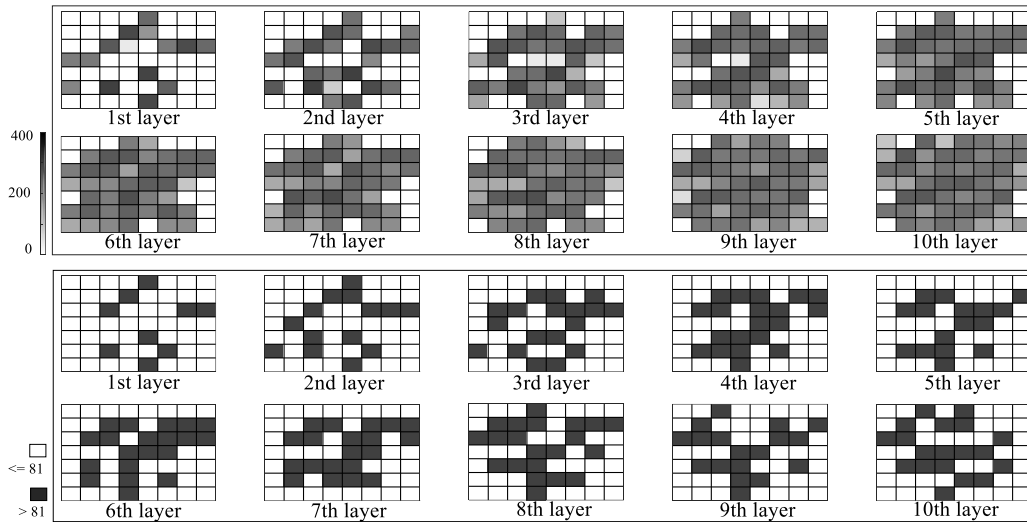
(b)

Fig. 3 Grayscale graph of number of signal rays passing through each voxel and distribution of voxel with sufficient signal rays (a and b stand for a rainless and a rainy day, respectively)

To better analyze the ill-conditioned nature of the observation equation in tomography modelling, the number of zero elements in matrix *A* is counted. We found that the proportion of zero element is over 97% in all tomographic solutions. In addition, the concept of matrix condition number is introduced to measure the degree of dispersion of the eigenvalues of the coefficient matrix (Edelman, 1989). The larger the value of the condition number, the more ill-conditioned the matrix is. The results show that the condition number in every tomographic solution is INF which means a serious ill-conditioned problem.

3.3 Internal Accuracy Testing

To evaluate the performance of water vapor tomography based on genetic algorithm, slant water vapor of GPS stations for the data of 13 to 19 August and 12 to 18 June, 2017 were computed using the tomographic results based on the water vapor tomographic observation equation established in Eq. (1). In this process, the parameters on the right side of Eq. (1) (the distance of the signal ray in each of the voxels and the water vapor density calculated by the tomographic modelling) are taken as known quantities. Moreover, the SWV on the left is the parameter to be determined, i.e. the tomography-computed SWV. The differences against the GAMIT-estimated SWV (as a reference) were also identified.

For internal accuracy testing, 13 GPS stations used in the tomographic modelling were adopted. The change of tomography computed VS GAMIT-estimated slant water vapor residuals with elevation angle is shown in Fig. 4, where the blue and red dots represent the rainy and rainless days, respectively. The maximum residuals for rainy and rainless scenarios are 10.74 and -9.84 mm, respectively. The root mean square error (RMS) and mean absolute error (MAE) for rainy and rainless days are 1.56/0.98 and 1.48/0.89mm, respectively. Fig. 4 shows that most of the residuals are concentrated between -2.0 and 2.0 mm which indicates good internal accuracy.
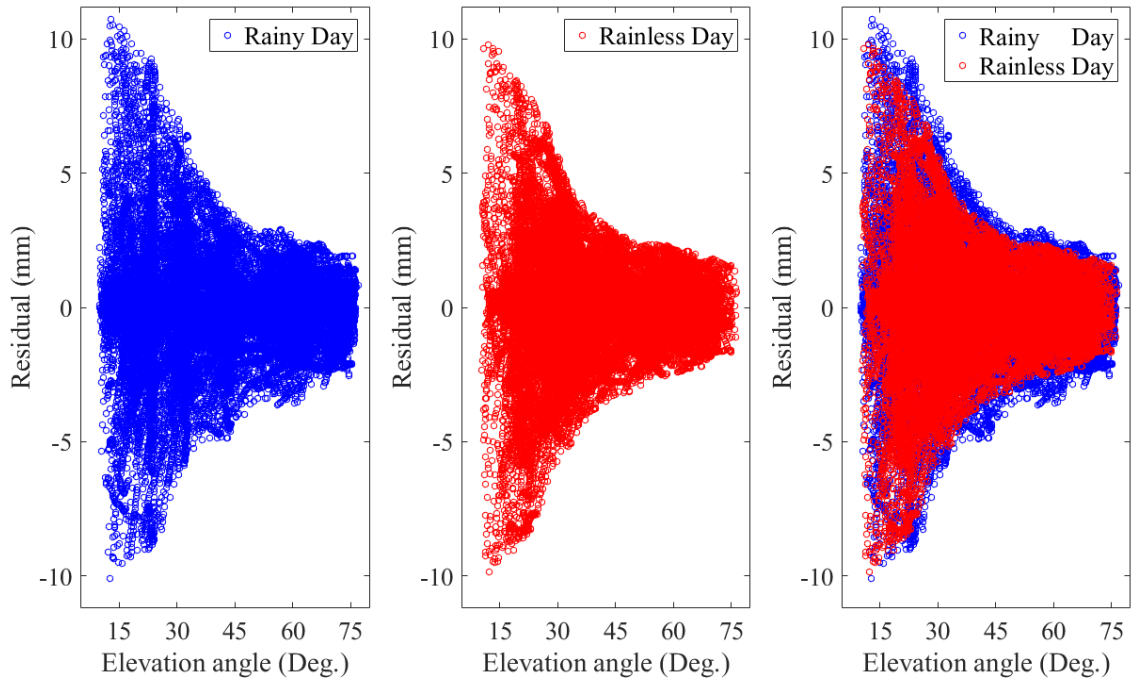
Fig. 4 Scatter diagram of the SWV residuals in different weather conditions for internal accuracy testing

To normalize SWV residuals for their evaluation in a single unit, we mapped the tomography-computed SWVs back to the zenith direction using the $1/\sin(e)$ formula and computed their differences with the GAMIT-estimated PWV (Michal et al.,

5   2017). Fig. 5 shows the statistical results of the residuals in the zenith direction. In the figure, the colours indicate the weather conditions (blue for rainy days and red for rainless days), and the 13 stations were arranged in the order in which they were added to the tomographic model. The maximum and minimum RMS in the two period are 0.79 and 1.81 mm, respectively, whereas the maximum and the minimum values for MAE are 0.43 and 1.54 mm, respectively. The RMS and MAE of rainless days are better than those of rainy day in each station. The medians of RMS and MAE are displayed for 13

10   stations to highlight differences among the stations. A particular outlier is the HKMW station, with RMS and MAE values 1.81/1.53 and 1.81/1.53 and 1.60/1.23 mm in rainy and rainless days, respectively. The reason for the divergent behaviour may be that two stations (HKPC and HKMW) exist in the same voxel which may result in the station (HKPC) data first introduced into the tomographic model affecting the subsequent station (HKMW) data. This hypothesis will be further investigated in future research. However, plots with RMS and MAE are consistent within 2.0 mm among all the stations (1.5

15   mm except for HKMW).
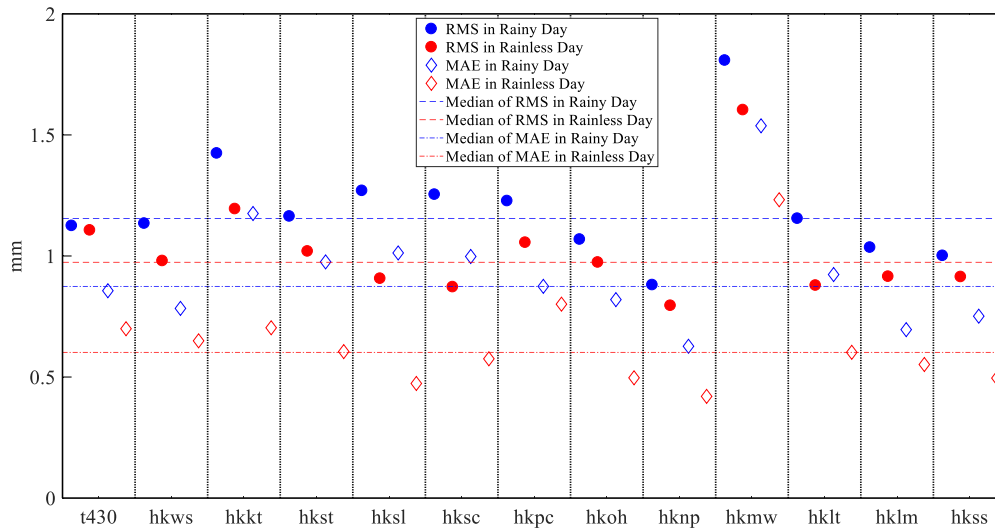
Fig. 5 Comparison of SWV residuals in zenith direction, circles for RMS and diamonds for MAE, blue for rainy days and red for rainless days.

3.4 External Accuracy Testing

5   For external accuracy testing, the data from KYC1 station which was not included in the tomographic modelling were used. Figure 6 shows the histogram for MAE (upper) and RMS (lower) of SWV residuals (differences between the tomography-computed SWV and GAMIT-estimated SWV), in which the blues and reds represent rainy and rainless days, respectively. The dashed bars are the averages for those different weather conditions. From this figure, it can be noted that all MAE and RMS are below 15mm, with average values lower for rainless days than for rainy days, respectively 8.75/7.33 and

10   11.38/9.54mm for RMS/MAE. Therefore, a good external accuracy is achieved by tomographic solutions considering the low RMS and MAE of rainy and rainless days.
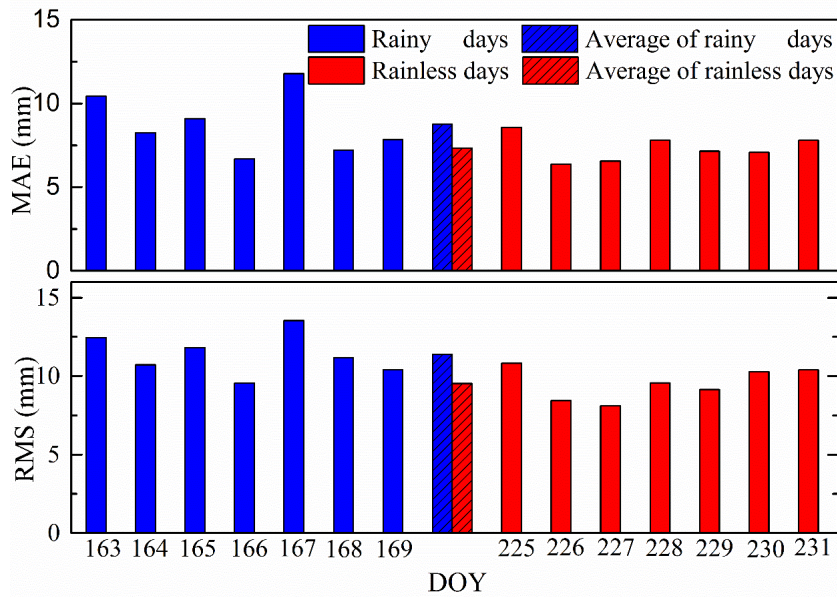
Fig. 6 Histogram for MAE (upper) and RMS (lower) of SWV residuals (differences between the tomography-computed SWV and GAMIT-estimated SWV) for the KYC1 station, which has not been used in the tomographic modelling (blue for rainy days, red for rainless days)
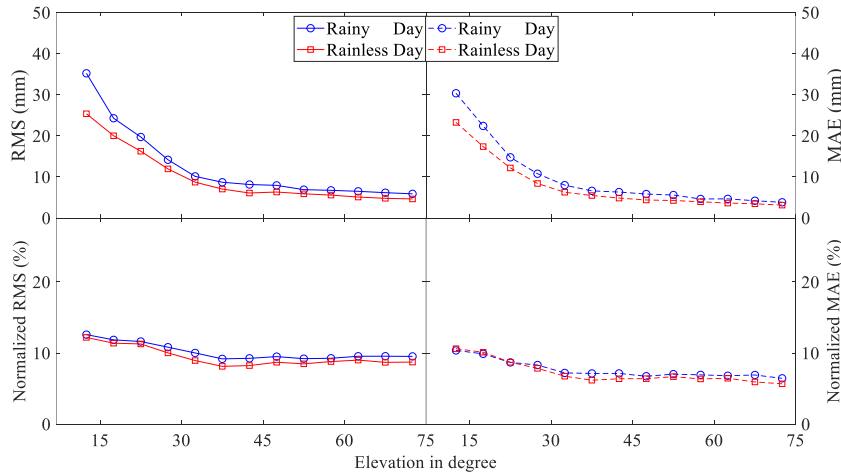
Fig. 7 Comparison of SWV residuals (differences between the tomography-computed SWV and GAMIT-estimated SWV) for the KYC1 station in each elevation bin, upper for RMS/MAE, lower for normalised RMS/MAE.

To further asses external accuracy, slant water vapor outputs were grouped into individual elevation bins of 5°, i.e. all SWVs with an elevation angle between 10° and 15° were evaluated as a single unit. The RMS and MAE of each elevation bin were calculated. To examine the dependence of relative errors in SWVs at different elevations, normalized RMS and MAE were computed. For this computation, residuals of SWV were divided by the GAMIT-estimated SWV and multiplied by 100 to obtain the percentages. Fig. 7 shows the variation of RMS, MAE, normalized RMS and normalized MAE as the elevation

angle changes in different weather conditions. For the upper figures, the RMS and MAE reduction of SWV residuals are clearly visible as the increasing elevation angle, which is consistent with the trend shown in Fig. 4. The colours in the figure indicate that better RMS and MAE results can be achieved on a rainless day than on a rainy day in each elevation bin. In terms of normalized RMS and MAE, we note that they remain almost constant over all elevation angles, indicating a

5   consistent relative performance of computing SWV in each type of weather condition. It is noted that the normalized RMS and MAE of rainless days are close to those of rainy days which may be due to the large SWV during rainy days that introduced a large denominator in the normalized calculation. Therefore, the good performance on relative error in SWVs at different elevations with a low normalized RMS/MAE (<0.125 for normalized RMS and <0.106 for normalized MAE) points to good external accuracy.

10   In the above analysis, RMS and MAE were used for the external accuracy testing of the tomographic results based on the GA. Box plots are used to explore the statistical characteristics of SWV residuals and to detect the outliers in the tomographic errors. Five characteristic values are shown in the box plots. Q1 and Q3 located at the bottom and top of the box represent the first and third quartiles; the second quartile (Q2) is located inside the box; the ends of the whiskers refer to the upper and lower bounds, which are located at Q1-1.5(IQR) and Q3+1.5(IQR), respectively. IQR is the interquartile range,

15   defined as the difference between Q3 and Q1, reflects the discreteness of a set of data. In Fig. 8 the length of box and the range of bound in rainless days (in red) are smaller than those in rainy days (in blue), indicating better residual distribution in rainless days than in rainy days. The right plots (in green) denote the result of combination of rainless and rainy days, representing the overall distribution of SWV residuals of tomography based on genetic algorithm. In our experiments, 50 % of the residuals are concentrated between -7.08 and 4.47 mm, and only 3.24% of the residuals are outliers when combining

20   the data of rainy and rainless days.
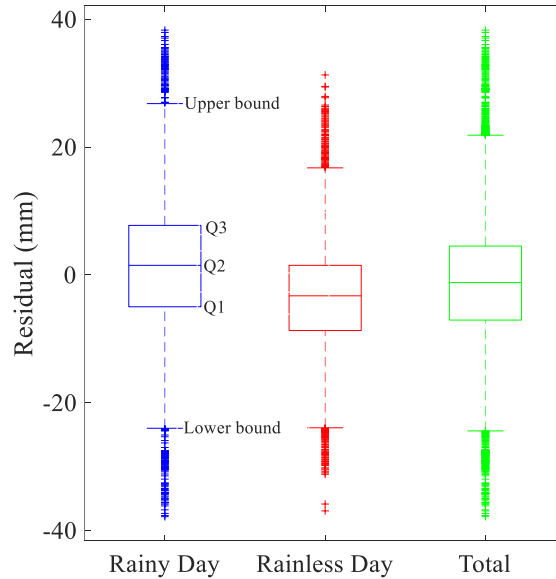
Fig. 8 Box plots of the SWV residuals (differences between the tomography-computed SWV and the GAMIT-estimated SWV) for the KYC1 station

3.5 Comparison with Radiosonde Data
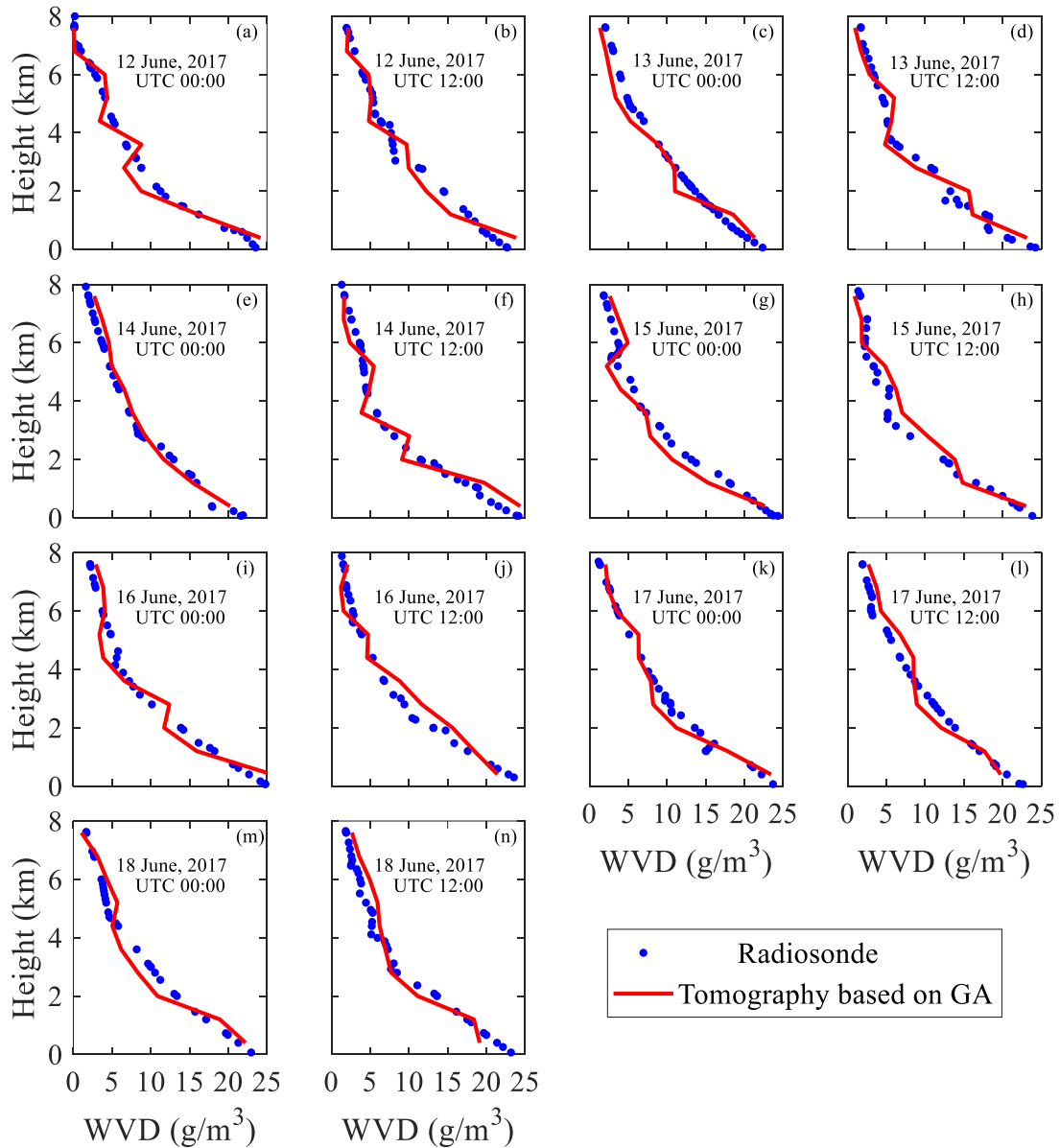
5   **Fig 9 (a-n)** represent water vapor density comparisons between radiosonde and tomography based on the genetic algorithm at UTC 0:00 and 12:00 from 12 to 18 June, 2017 (rainy days)

The water vapor density profile derived from the radiosonde data can be used as a reference value, which is well suited to evaluate the accuracy of the tomographic results based on genetic algorithm. As the radiosondes are launched daily at 00:00 and 12:00 UTC, the tomographic results of 12 to 18 June (rainy days) and 13 to 19 August, 2017 (rainless days) at these times were compared. Figure 9 shows the water vapor density comparisons between radiosonde data and tomographic results for different altitudes at individual dates (rainy period). It is clear from the profiles that the WVD decreases with increasing height. The WVD profiles reconstructed by the GA tomographic solutions conform with those derived from the radiosonde data, especially in the upper troposphere in absolute terms. With respect to the relative error, the values of the voxels upper than 5km and lower than 5km are 31% and 15%, respectively. The reason for this phenomenon is that the value of water vapor in the upper layers is relatively low. Even a small difference between the radiosonde and tomographic result can also lead to a large relative error, whereas the water vapor content resides for more than 90% below 5km near the Earth's surface. In certain cases, a relatively good consistency can also be seen in the lower atmosphere. This may be because a GPS station (HKSC) for tomography modelling is located at the voxel where the radiosonde station is situated, resulting in the low atmosphere with sufficient signal rays passing through.

Table 2 RMS and MAE of the water vapor density comparison between radiosonde and tomography based on the genetic algorithm for different weather conditions (g/m³)

Weather condition	Date	RMS		MAE	
		UTC 0:00	UTC 12:00	UTC 0:00	UTC 12:00
Rainy days	12 June	1.54	1.68	1.27	1.43
	13 June	1.20	1.57	1.81	1.39
	14 June	1.37	1.79	0.85	1.56
	15 June	1.63	1.38	1.41	1.27
	16 June	1.77	1.48	1.56	1.31
	17 June	1.49	1.33	1.55	1.18
	18 June	1.52	1.38	1.34	1.22
	Average	1.51		1.29	
Rainless days	13 August	1.44	1.35	1.14	0.93
	14 August	1.46	1.25	1.18	1.05
	15 August	1.54	1.27	1.26	0.83
	16 August	1.29	1.14	1.03	0.89
	17 August	1.38	1.39	1.09	1.24
	18 August	1.46	1.26	1.19	1.06
	19 August	1.23	1.40	1.03	1.19
	Average	1.35		1.08	

	Total	1.43	1.19

To further illustrate the comparison with the radiosonde data, Table 2 listed RMS and MAE of the WVD. In the table, the WVD in the voxels above the radiosonde station computed by tomography and those derived from radiosonde are counted to calculate their RMS and MAE in each solution. Thus, the average RMS/MAE of rainless days are 1.35/1.08 g/m^3, which is smaller than 1.51/1.29 g/m^3 in rainy days. This finding is consistent with the comparison of SWV above. We compare those

5   values with the results obtained from other Hong Kong tomographic experiments. For example, Xia et al. (2013) obtained an RMS of 1.01 g/m^3 by adding the COSMIC profiles as external data based on two-step reconstructions. Using the least squares method with horizontal and vertical constraints, Yao et al. (2016) obtained an RMS of 1.23 g/m^3 by maximally using GPS observations and an RMS of 1.60 g/m^3 without the operation. Zhao et al. (2017) achieved an RMS of 1.19 g/m^3 and 1.61 g/m^3 considering the signal rays crossing from the side of the research area and an RMS of 1.79 g/m^3 without this

10   consideration. Yao et al. (2017) achieved an RMS from 1.48-1.80 g/m^3 using different voxel division approaches. Using the ART with empirical value 0.24 as relaxation parameter, Ding et al. (2017) obtained an RMS of 1.23 g/m3 and 1.45 g/m3 by utilizing the new parametric methods based on inverse distance weighted (IDW) interpolation and the traditional methods. Note that the RMS calculated in the above experiments are based on the radiosonde data. Therefore, the total RMS of 1.43 g/m^3 for the two time periods in this paper can be considered in a good agreement with the radiosonde data regardless of the

15   weather conditions. Moreover, many different settings are applied in tomographic experiments by different groups, such as the selection of tomographic boundary, differences of experimental period and weather condition, division rule of horizontal and vertical voxel, addition of other observations.
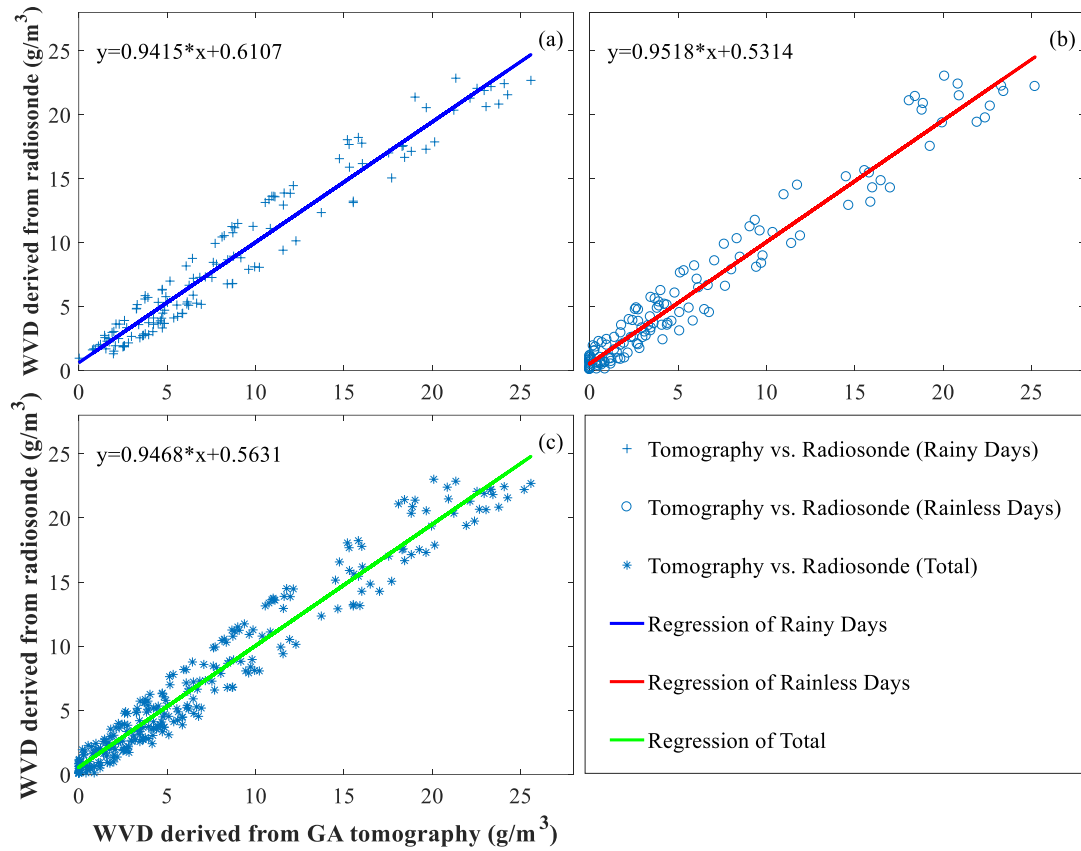
Fig. 10 Linear regression of the water vapor density from radiosonde and tomography based on the genetic algorithm. (a), (b) and (c) represent rainy days, rainless days and their combination, respectively.

To explore the overall accuracy of water vapor density reconstructed by the GA tomography, the linear regression analysis and box plot were adopted for different weather conditions. Figure 10 shows the linear regression of the water vapor density for rainy days (a), rainless days (b) and their combination (c), in which the scatter points of three graphs are close to the 1:1 lines. In comparison with the coefficients of regression equations, the results from rainless days are slightly better than those of rainy days. When combining the data of two periods, the starting point of the regression equation is 0.5631 and the slope is 0.9468, water vapor density can be achieved with high accuracy by tomography based on the GA. The corresponding box plots are shown in Fig. 11. It can be noted that the WVD residuals are concentrated in the range of -2 to 2 mm, and the rainless scenario is better than the rainy scenario. The Q1/Q3 are -1.28/1.08, -1.20/0.65 and -1.24/0.87 mm for rainy days, rainless days and their combination, respectively. The upper and lower boundaries are located near 4 and -4mm. No outlier is present in this box plots probably due to few WVD residuals.
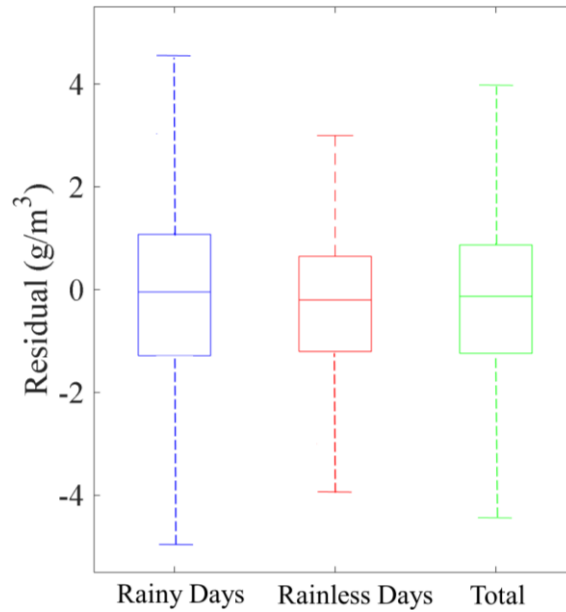
Fig. 11 Box plots of the WVD residuals, which are computed between GA tomographic approach and radiosondes.

3.6 Comparison with tomographic results of the Least Squares method

The Least squares method is most commonly used in water vapor tomography, and numerous experiments prove that water vapor density with high accuracy can be obtained with this method (Flores, et al., 2000; Zhang et al., 2017; Zhao et at., 2017). To verify the accuracy of the genetic algorithm, we compared the tomographic results between the genetic algorithm and the least squares method in this section. The specific process and introductions of the least squares method can be found in detail in e.g. Flores et al. (2000), Guo et al. (2016) and Yang et al. (2018). Figure 12 shows the three-dimensional distribution of water vapor density derived from tomography based on the GA and the least squares method. The water vapor computed by the European Centre for Medium-Range Weather Forecasts (ECMWF) data, which provides various meteorological parameters at different pressure levels with a spatial resolution of 0.125°*0.125°, is displayed in the figure as a reference. Here both the GA and the least squares method give a reasonable tomographic result. In certain voxels, the GA achieves the closer results to the ECMWF data, whereas for other voxels, the least squares method performs better. Both methods (the GA and the least squares) generally have a good consistency with ECMWF data regardless of the weather conditions, and can accurately describe the spatial distribution of water vapor. Additionally, a larger variation of water vapor with altitude occurs in a rainy scenario than in a rainless scenario, especially in the upper atmosphere, which is well captured by the GA and the least squares method. Numerical results including RMS and MAE during the whole experimental period are listed in Table 3 to show the comparison of the GA and the least squares method, in which the water vapor density derived from ECMWF data is regarded as the true value. It indicates that the result of the GA is a little better than that of least squares method.
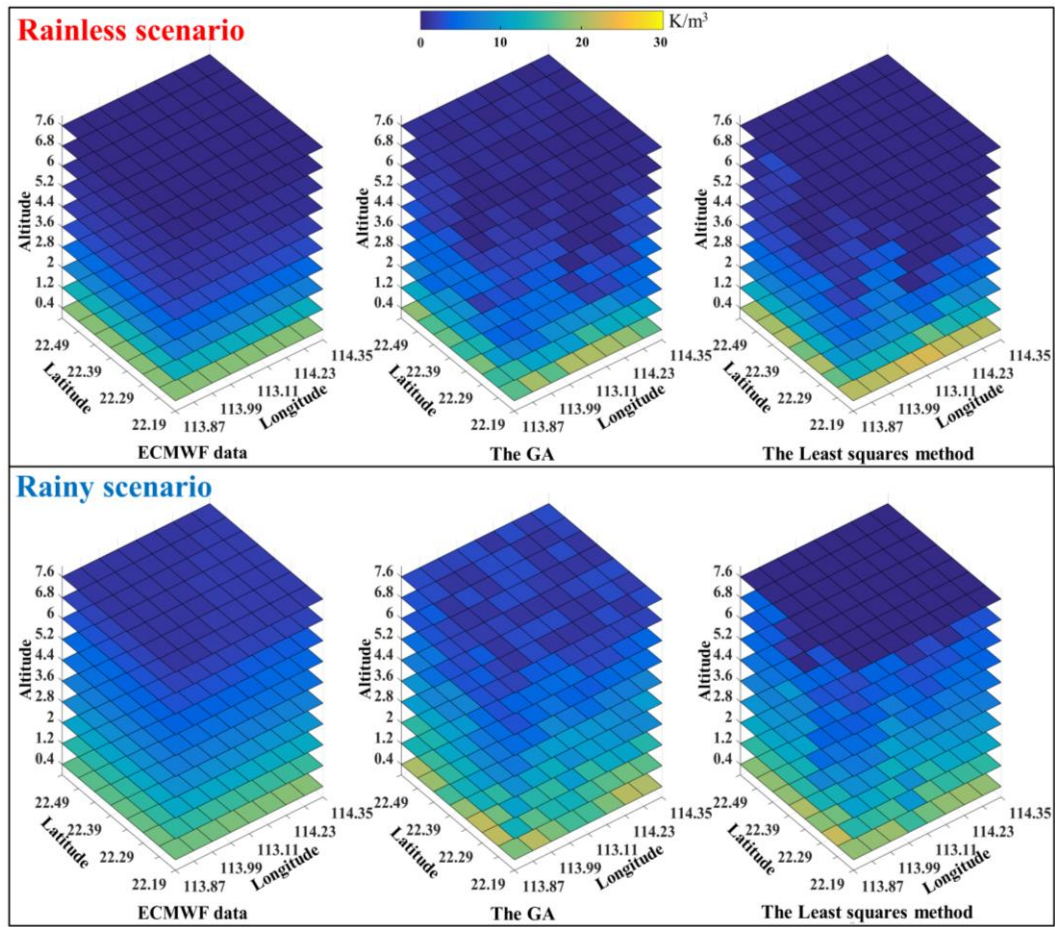
Fig. 12 The three-dimensional distribution of water vapor density derived from ECMWF data, the GA method and the Least squares method (upper for rainless scenario and lower for rainy scenario)

Table 3 Statistical results of the GA and the Least squares method comparison, ECMWF data as a reference (g/m^3)

	GA method		Least squares method	
	RMS	MAE	RMS	MAE
Rainy scenario	1.84	1.42	1.94	1.47
Rainless scenario	1.71	1.39	1.79	1.37
average	1.78	1.41	1.87	1.42

To further analyze the tomographic results of the GA and the least squares method, regression and boxplot are conducted and displayed in Figure 13, which covers all solutions, each of them containing 560 voxel results. In the left panel, a good linear regression relationship is shown by the distribution of scatter points and the straight line of regression. Specifically, the starting points of the regression equation and the slop are 0.5198 and 0.9401, respectively. The right panel shows the

distribution of differences between the two types of tomographic results. The Q1 and Q3 are -0.84 and 0.60 g/m^3, which means that more than 50% of the differences between the two methods are within 1 g/m^3. The upper and lower bounds are 2.75 and -2.98 g/m^3, respectively, and outliers only account for 3.11%. Consequently, the tomographic results based on the GA are in agreement with those of the least squares method for this experiment. A reliable tomographic result can be achieved by the GA without being restricted by constraint equations and matrix inversion like the traditional least squares method.
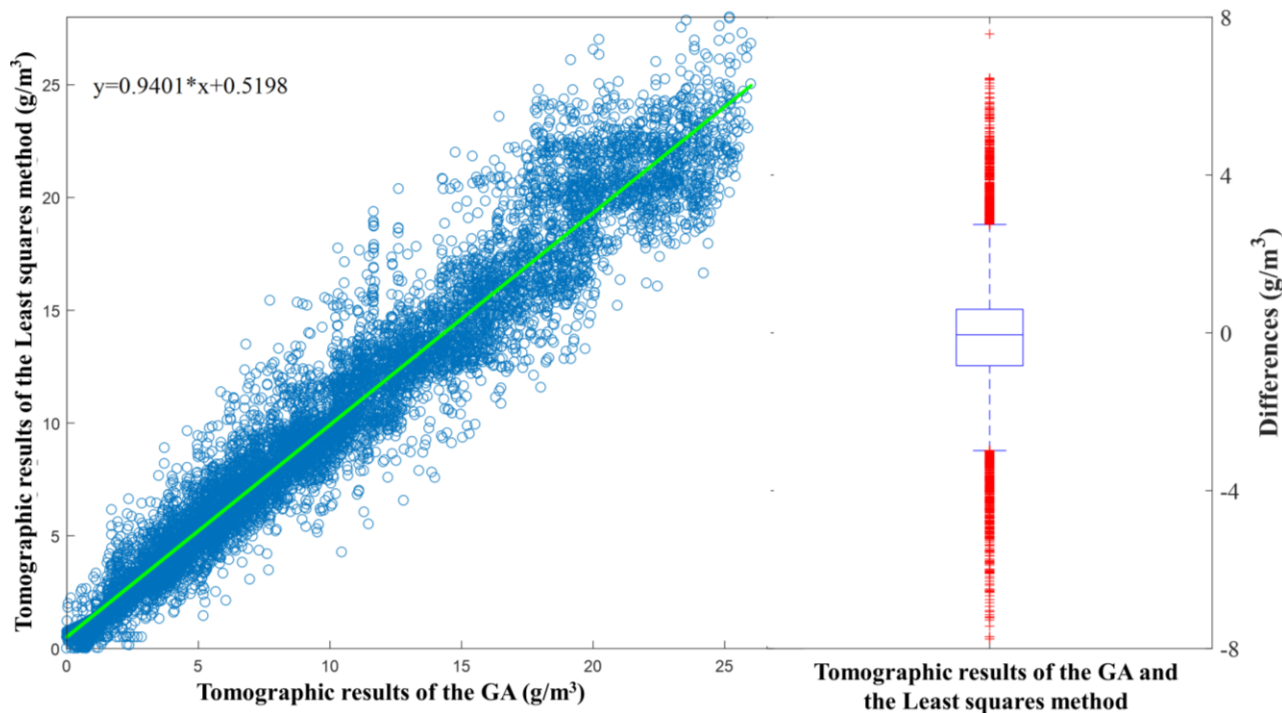
Fig. 13 Regression (left) and boxplot (right) for tomographic results (WVD) of the GA and the Least squares method

Moreover, a detailed comparison between GA and Least squares method is conducted using the voxels above the radiosonde station. Fig. 14 shows the changes of water vapor density derived from GA and Least squares method with altitudes in different days (rainless days), in which the radiosonde data and ECMWF data are considered as reference data. All the profiles derived from the two methods decrease with increasing height and show good consistency with the reference data. The statistical values are computed and listed in Table 4 to illustrate the comparison of GA and Least squares method. The RMS and MAE indicate that both the GA and Least squares method can achieve good tomographic results compared with the reference values (radiosonde and ECMWF data) whether in the rainy or rainless scenario. The GA which has an average RMS/MAE of 1.43/1.19 and 1.30/1.05 g/m^3 compared with radiosonde and ECMWF data, respectively performs slightly better than the Least squares method, of which the average RMS/MAE are 1.49/1.23 and 1.36/1.12 g/m^3.
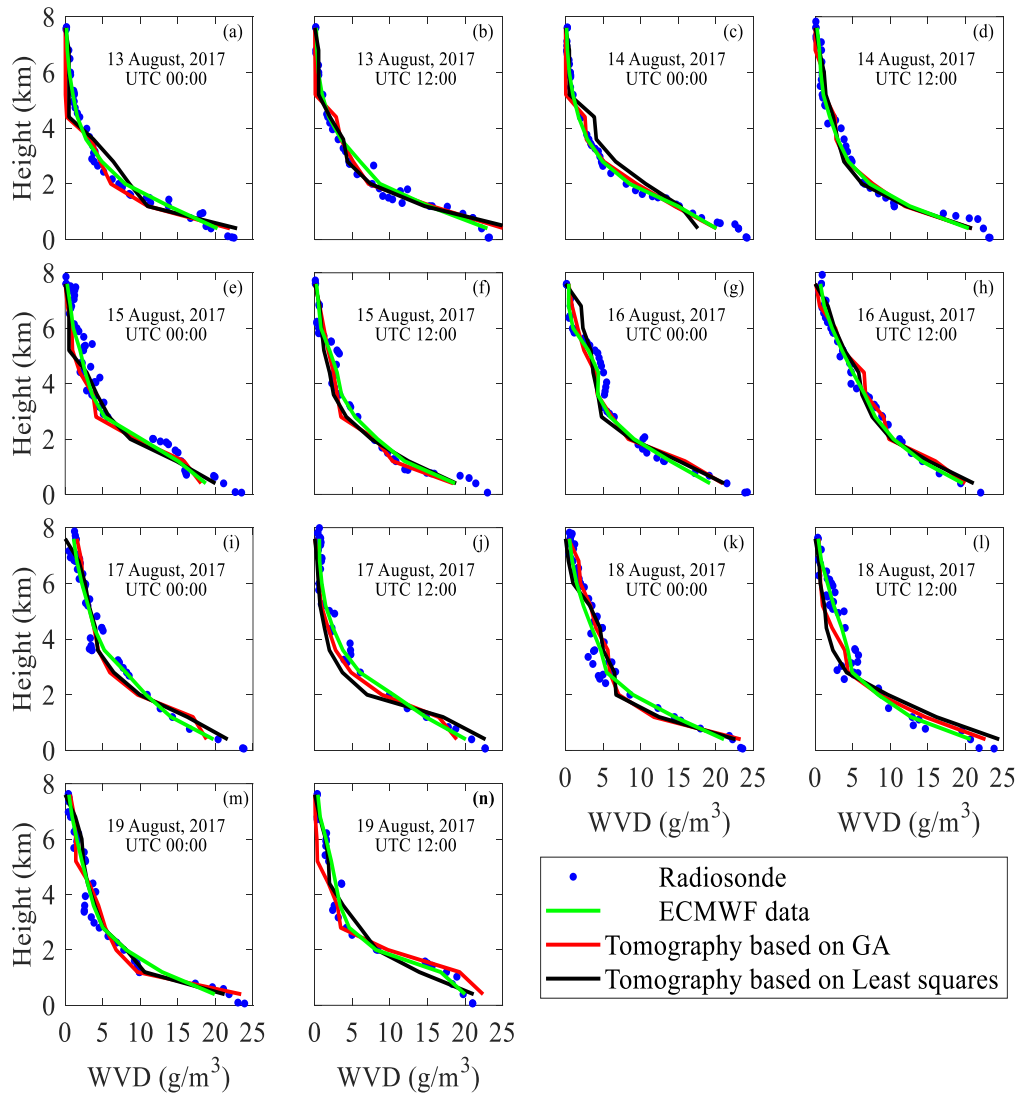
Fig. 14 Water vapor density comparisons between GA and Least squares method in the selected voxels at UTC 0:00 and 12:00 from 13 to 19 August ,2017 (rainless days), radiosonde and ECMWF data are used as reference.

Table 4 Statistical results of the GA and the Least squares method using radiosonde and ECMWF data as reference in the selected voxels (g/m³)

Data comparison	Rainy Days		Rainless Days		Average	
	RMS	MAE	RMS	MAE	RMS	MAE
Radiosonde vs GA	1.51	1.29	1.35	1.08	1.43	1.19
Radiosonde vs Least squares method	1.58	1.34	1.40	1.16	1.49	1.25

ECMWF vs GA	1.35	1.12	1.25	0.97	1.30	1.05
ECMWF vs Least squares method	1.43	1.20	1.29	1.03	1.36	1.12

3.7 Analysis of results in different weather conditions
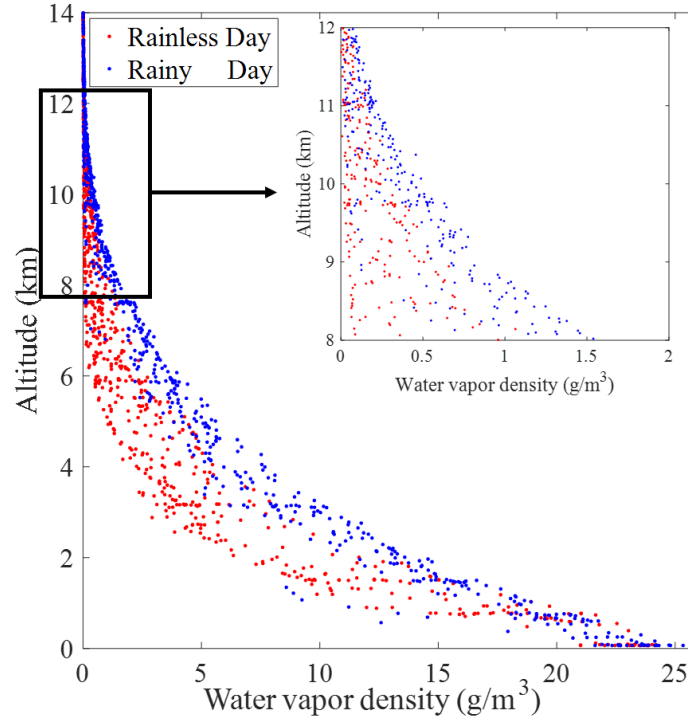
Fig. 15 Changes of water vapor density with altitude in different weather conditions, data from radiosonde (blue for rainy days from 12 to 18 June, 2017 and red for rainless days from 13 to 19 August, 2017)

5   In our experiments, the comparison under various weather conditions illustrate that tomographic result of rainless scenarios was better than of rainy scenarios, which is also concluded in other studies (Yao et al., 2016, Zhao et al., 2017 and Ding et al., 2017). This result is because the spatial structure of atmospheric water vapor is relatively stable in rainless weather, whereas its spatial distribution changes faster in rainy weather. Thus, certain limitations are imposed on tomography to obtain accurate water vapor during unstable weather conditions. Additionally, all the water vapor densities along the

10   radiosonde path were collected during the experiments. Their changes with altitude are shown in Fig. 15, in which the rainy and rainless weather are represented by blue and red dots. The situation of 8-12 km is magnified to show the water vapor information outside the tomographic region. In the figure, the larger value of WVD can be observed above 8 km in rainy days compared with that of rainless days. For the rainless situation, the value of WVD within 8-12 km is small and near to zero. By contrast, the value is basically not close to zero in the rainy situation, especially in the range of 8-10 km, which is

substantially greater than 0.5 g/m^3. Referring to the selection of the tomographic heights in other articles, considering the long-term statistics of water vapor in Hong Kong, and taking into account the drawbacks of the excessive number of tomographic voxels, we selected 8 km as the top boundary of the research area in this paper, which ignores the water vapor information above 8 km in our tomographic model. Obviously, it has limited influence on the accuracy of the tomographic result in rainless weather condition. For the rainy weather condition, the effect could be slightly large, which is one reason why the tomographic results of rainy days were worse than those of rainless days in our experiments.

4 Conclusions

In this paper, a new tomography approach based on the genetic algorithm was proposed to reconstruct a three-dimensional water vapor field in Hong Kong under rainy and rainless weather conditions. The inversion problem was transformed into an optimization problem that no longer depends on excessive constraints, a priori information and external data. Thus, many problems do not need to be considered, including the difficulty of inverting the sparse matrix, the limitation and irrationality of constraints, the weakening of tomographic technique by prior information, and the restriction of obtaining external data. Based on the fitness function established by the tomographic equation, the water vapor tomographic solution could be achieved by the genetic algorithm through the process of selection, crossover and mutation.

Our new approach is validated by tomographic experiments using GPS data collected over Hong Kong from 12 to 18 June (rainy days) and 13 to 19 August, 2017 (rainless days). The problem of matrix ill-condition was discussed and analysis by the grayscale graph and condition number. In a comparison of the SWV residuals, internal and external accuracy testing are used for the GA tomography. The internal accuracy testing refers to compute the differences between the tomography-computed SWV and GAMIT-estimated SWV for the 13 GPS stations used in the tomographic modelling, whereas the external accuracy testing denotes the differences for the KYC1 station which is not included in the tomographic modelling. The RMS/MEA of SWV residuals are 1.52/0.94 and 10.07/8.44 mm for the internal and external accuracy testing, respectively. Thus, good tomographic result is achieved. In addition, the water vapor density of the proposed method agreed with that of radiosonde. The RMS and MEA are 1.43 g/m^3 and 1.19 g/m^3, whereas the starting point and the slope of the regression equation are 0.5631 and 0.9468, respectively. ECMWF data are utilized to display the three-dimensional distribution of tomographic results. Least squares method is selected as the representative of traditional tomographic method to compare with the GA. A good consistency is demonstrated in terms of RMS, MAE, linear regression and boxplot. Thus, a reliable tomographic result can be achieved by the GA without being restricted by constraint equations and matrix inversion like the traditional least squares method. Moreover, the comparison under various weather conditions illustrated that tomographic result of rainless scenario was better than that of rainy scenario, and the reasons were discussed. In the future study, the tomography approach based on the genetic algorithm, which is not dependent on constraints, a priori data and external data, could provide potential interest for the establishment of real-time or near-real-time water vapor tomographic system.

Author contributions. Conceptualization, Fei Yang, Jiming Guo and Junbo Shi; Data curation, Yinzhi Zhao, Lv Zhou and Di Zhang; Formal analysis, Fei Yang, Jiming Guo and Junbo Shi; Methodology, Fei Yang; Resources, Junbo Shi, Xiaolin Meng; Validation, Fei Yang; Writing – original draft, Fei Yang; Writing – review & editing, Fei Yang, Jiming Guo, Xiaolin Meng, Junbo Shi, Lv Zhou, Yinzhi Zhao and Di Zhang.

Competing interests. The authors declare no conflict of interest.

Acknowledgement. This research was funded by [National Natural Science Foundation of China] grant number [41604019, 41474004]. The authors would like to thank the Lands Department of HKSAR for providing the GNSS data from the HONG
10   KONG Satellite Positioning Reference Station Network (SatRef). Chinese Scholarship Council (CSC) and the University of Nottingham for providing the opportunity for the first author to study at the University of Nottingham for one year. Acknowledgements are also given to the editor in charge (Roeland Van Malderen) and my colleague at the University of Nottingham (Simon Roberts) for their revision to improve the English language and style of the paper.

References

15   Adavi, Z. and Mashhadi-Hossainali, M.: 4D-tomographic reconstruction of water vapor using the hybrid regularization technique with application to the North West of Iran, Adv. Space Res., 55, 1845-1854, doi:10.1016/j.asr.2015.01.025, 2015.

Alber, C., Ware, R., Rocken, C., Braun, J.: Obtaining single path phase delays from GPS double differences, Geophys. Res. Lett., 27, 2661-2664, doi:10.1029/2000GL011525, 2000.

Astudillo, J., Lau, L., Tang, Y., Moore, T.: Analysing the Zenith Tropospheric Delay Estimates in On-line Precise Point
20   Positioning (PPP) Services and PPP Software Package, Sensors., 18, 580, doi:10.3390/s18020580, 2018.

Bar-Sever, Y. E., Kroger, P. M., Borjesson, J. A.: Estimating horizontal gradients of tropospheric path delay with a single GPS receiver, J. Geophys. Res.: Solid Earth, 103, 5019-5035, doi: 10.1029/97JB03534, 1998.

Bender, M., Dick, G., Ge, M., Deng, Z., Wicker, J., Kahle, H.-G., Raabe, A., Tetzlaff, G.: Development of a GNSS water vapor tomography system using algebraic reconstruction techniques, Adv. Space Res., 47, 1704–1720,
25   doi:10.1016/j.asr.2010.05.034, 2011.

Benevides, P., Nico, G., Catalao, J.: Merging SAR interferometry and GPS tomography for high-resolution mapping of 3D tropospheric water vapor, In Proceedings of the Geoscience and Remote Sensing Symposium, Milan, Italy, 26–31 July 2015.

Bevis, M., Businger, S., Herring, T. A., Rocken, C., Anthes, R. A., Ware, R. H.: GPS meteorology: Remote sensing of atmospheric water vapor using the Global Positioning System, J. Geophys. Res. Atmos., 97, 15787–15801,
30   doi:10.1029/92JD01517, 1992.

Braun, J., Rocken, C., Meetrens, C., Ware, R.: Development of a Water Vapor Tomography System Using Low Cost L1 GPS Receivers, 9th ARM Science Team Meeting, US Dep. of Energy, San Antonio, Texas, 22-26 March 1999.

Chen, B., Liu, Z.: Assessing the performance of troposphere tomographic modeling using multi-source water vapor data during Hong Kong's rainy season from May to October 2013, Atoms. Meas. Tech., 9, 1–23, doi:10.5194/amt-9-5249-2016, 2016.

Davis, J., Herring, T., Shapiro, II., Rogers, A., Elgered, G.: Geodesy by radio interferometry: Effects of atmospheric
5   modeling errors on estimates of baseline length, Radio Sci., 20, 1593-1607, doi:10.1029/RS020i006p01593, 1985.

Ding, N., Zhang, S., Zhang, Q.: New parameterized model for GPS water vapor tomography, Ann. Geophys., 35, 311-323, doi: 10.5194/angeo-35-311-2017, 2017.

Dong, Z., Jin, S.: 3-D water vapor tomography in Wuhan from GPS, BDS and GLONASS observations, Remote Sens., 10, 62, doi:10.3390/rs10010062, 2018.

10 Dwivedi, R., Dikshit, O.: A comparison of particle swarm optimization (PSO) and genetic algorithm (GA) in second order design (SOD) of GPS networks, J. Appl. Geodesy., 7, 135-145, doi:10.1515/jag-2013-0045, 2013.

Edelman, A.: Eigenvalues and condition numbers of random matrices, Siam J. Matrix Anal. Appl., 9, 543–560, doi:10.1137/0609045, 1989.

Flores, A., Ruffini, G., Rius, A.: 4D tropospheric tomography using GPS slant wet delays, Ann. Geophys., 18, 223–234,
15 doi:10.1007/s00585-000-0223-7, 2000.

Goldberg, D.: Genetic Algorithm in Search Optimization and Machine Learning, Addison Wesley., 7, 2104-2116, 1989.

Guo, J., Yang, F., Shi, J., Xu, C.: An optimal weighting method of Global Positioning System (GPS) troposphere tomography, IEEE J. Sel. Top. Appl. Earth Obs. Remote Sens., 9, 5880–5887, doi:10.1109/JSTARS.2016.2546316, 2016.

Guo, Q., Hu, Z.: Application of genetic algorithm to solve ill-conditioned equations for GPS rapid positioning, Geomatics
20 Inf. Sci. Wuhan Univ., 34, 230-243, 2009.

Holland, J.: Adaptation in Natural and Artificial Systems. University of Michigan Press, Ann Arbor, Michigan; re-issued by MIT Press, 1992.

Kacmarík, M., Douša, J., Dick, G.: Inter-technique validation of tropospheric slant total delays, Atoms. Meas. Tech., 10, 2183-2208, doi: 10.5194/amt-10-2183-2017, 2017.

25 Liu, J., Sun, Z., Liang, H., Xu, X., Wu, P.: Precipitable water vapor on the Tibetan Plateau estimated by GPS, water vapor radiometer, radiosonde, and numerical weather prediction analysis and its impact on the radiation budget, J. Geophys. Res. Atmos., 110, 1-12, doi:10.1029/2004JD005715, 2005.

Liu, S. Z., Wang, J. X., Gao, J. Q.: Inversion of ionosphere electron density based on a constrained simultaneous iteration reconstruction technique, IEEE T. Geosci. Remote, 48, 2455-2459, 2010.

30 Liu, Y., Chen, Y., Liu, J.: Determination of weighted mean tropospheric temperature using ground meteorological measurement, Geo-Spat, Inf. Sci., 4, 14–18, doi:10.1007/BF02826630, 2001.

Nilsson, T. and Gradinarsky, L.: Ground-Based GPS Tomography of Water Vapor: Analysis of Simulated and Real Data, J. Meteorol. Soc. Jpn., 82, 551-560, doi:10.1109/TGRS.2006.877755, 2004.

Nilsson, T., Gradinarsky, L.; Elgered, G. GPS tomography using phase observations. In Proceedings of the 2004 IEEE International Geoscience and Remote Sensing Symposium, Anchorage, AK, USA, 20–24 September, 2756–2759, 2004.

Olinsky, A., Quinn, J., Mangiameli, P., Chen, S.: A genetic algorithm approach to nonlinear least squares estimation, Int. J. Math. Educ. Sci. Technol., 35, 207-217, doi:10.1080/00207390310001638331, 2004.

5   Perler, D., Geiger, A., Hurter, F.: 4D GPS water vapor tomography: new parameterized approaches, J. Geodesy., 85, 539-550, doi:10.1007/s00190-011-0454-2, 2011.

Rocken, C., Ware, R., Van Hove, T., Solheim, F., Alber, C., Johnson, J.: Sensing atmospheric water vapor with the global positioning system. Geophys, Res. Lett., 20, 2631–2634, doi:10.1029/92JD01517, 1993.

Rohm, W., Zhang, K., Bosy, J.: Limited constraint, robust Kalman filtering for GNSS troposphere tomography, Atoms.
10 Meas. Tech., 7, 1475-1486, doi:org/10.5194/amt-7-1475-2014, 2014.

Rohm, W.: The precision of humidity in GNSS tomography, Atmos. Res., 107, 69–75, doi:10.1016/j.atmosres.2011.12.008, 2012.

Saastamoinen, J.: Atmospheric correction for the troposphere and stratosphere in radio ranging satellites, Use Artif. Satell. Geodesy., 247-251, doi:10.1029/GM015p0247, 1972.

15 Song, S., Zhu, W., Ding, J., Peng, J.: 3D water vapor tomography with Shanghai GPS network to improve forecasted moisture field, Chin. Sci. Bull., 51, 607–614, doi:10.1007/s11434-006-0607-5, 2006.

Stolle, C., Schluter, S., Heise, S., Jacobi, N., Raabe, A.: A GPS based three-dimensional ionospheric imaging tool: Process and assessment, Adv. Space Res., 38, 2313-2317, 2006.

Venkatesan, R., Krishnan, T., Kumar, V.: Evolutionary estimation of macro-Level diffusion models using genetic algorithms:
20 an alternative to nonlinear least squares, Marketing Science., 23, 451-464, doi:10.1287/mksc.1040.0056, 2004.

Wang, J., Pin, L., Chen, W.: An interferometric calibration method based on genetic algorithm for InSAR system, J. Univ. Sci. Technol. China., 40, 133-139, doi:10.3969/j.issn.0253-2778.2010.02.005, 2010.

Wang, X., Dai, Z., Zhang, E., Fuyang, K., Cao, Y., Song, L.: Tropospheric wet refractivity tomography using multiplicative algebraic reconstruction technique, Adv. Space Res., 53, 156-162, doi:10.1016/j.asr.2013.10.012, 2014.

25 Xia, P., Cai, C., Liu, Z.: GNSS troposphere tomography based on two-step reconstruction using GPS observation and COSMIC profiles, Ann. Geophys., 31, 1805–1815, doi:10.5194/angeo-31-1805-2013, 2013.

Yang, F., Guo, J., Shi, J., Zhou, L., Xu, Y., Chen, M.: A method to improve the distribution of observations in GNSS water vapor tomography, Sensors., 8, 2526, doi:10.3390/s18082526, 2018.

Yao, Y., Zhao, Q., He, Y., Li, Z.: A three-dimensional water vapor tomography algorithm based on the water vapor density
30 scale factor, Acta Geodaetica et Cartographica Sinica, 45, 260-266, doi: 10.11947/j.agcs.2016, 2016.

Yao, Y., Zhao, Q.: A novel, optimized approach of voxel division for water vapor tomography, Meteorol Atmos Phys , 129, 57-70, doi: 10.1007/s00703-016-0450-4, 2017.

Yao, Y., Zhao, Q.: Maximally using GPS observation for water vapor tomography, IEEE Trans. Geosci. Romote Sens., 54, 7185-7196, Doi: 10.1109/TGRS.2016.2597241, 2016.

Zhang, B., Fan, Q., Yao, Y., Xu, C., Li, X.: An Improved Tomography Approach Based on Adaptive Smoothing and Ground Meteorological Observations, Remote Sens., 9, 886, doi:10.3390/rs9090886, 2017.

Zhao, Q., Yao, Y., Yao, W.: A troposphere tomography method considering the weighting of input information, Ann. Geophys., 35, 1327-1340, doi: 10.5194/angeo-35-1327-2017, 2017.

5   Zhao, Q., Yao, Y.: An improved troposphere tomographic approach considering the signals coming from the side face of the tomographic area, Ann. Geophys, 35, 143-152, doi:10.5194/angeo-35-87-2017, 2017.